# Is the Karman Mode the Least Stable Mode Below the Critical Re?

**Sushil Mohan Ratnaker[1] and Sanjay Mittal[1,2]**

**Abstract:** Flow past a circular cylinder looses stability at $Re \sim 47$ via Hopf bifurcation. The eigenmode responsible for the instability leads to the von Kármán vortex shedding. In this work the linear stability of the flow to other modes, near the critical $Re$, is investigated. In particular, the study explores the possibility of modes other than the Kármán mode having the largest growth rate for $Re < Re_{cr}$. To this extent, global linear stability analysis ($LSA$) of the steady flow past a circular cylinder is carried out for $Re = 45$ and 48. In addition to the Kármán modes, two other modes are tracked. The eigenvalue of one of them is associated with a very small imaginary part; the mode is referred to as the $St \rightarrow 0$ mode. The Strouhal number, $St$, is the non-dimensional vortex shedding frequency and is related to the imaginary part of the eigenvalue. The other mode is real and is referred to as the $St = 0$ mode. The modes also differ in regard to their symmetry about the wake centerline. Unlike the Kármán mode, the two modes are very sensitive to the spatial extent of the computational domain. Computations are carried out with domains of varying spatial extent and their results are utilized to estimate the growth rate and $St$ for the unbounded flow. All the modes are stable for the $Re = 45$ flow. Of the three modes, the Kármán mode is most stable. Interestingly, the $St \rightarrow 0$ mode is found to be least stable. For the $Re = 48$ flow, the $St \rightarrow 0$ mode is most stable followed by the $St = 0$ mode. The computations are utilized to determine the least stable mode for various $Re$. The Kármán mode has the largest growth rate for $Re \geq 47.05$ while the $St \rightarrow 0$ mode is the least stable mode for $Re \leq 46.59$. The $St = 0$ mode dominates for $46.59 < Re < 47.05$. The results from the LSA are confirmed via direct time integration ($DTI$) of the linearized equations.

**Keywords:** Linear stability analysis, Direct time integration, Stabilized finite element method, Mode cross-over, Subspace iteration, Arnoldi method.

---

[1] Department of Aerospace Engineering, Indian Institute of Technology Kanpur, Kanpur, U.P., India – 208 016

[2] smittal@iitk.ac.in, Phone: +91 512 2597906, Fax: +91 512 2597561

## 1   Introduction

The instability of steady, incompressible viscous flow past a circular cylinder has been investigated in several research efforts in the past. Its importance in theoretical studies as well as in engineering applications can hardly be exaggerated. Flow past a circular cylinder becomes unstable beyond $Re \sim 47$ [Kumar and Mittal (2006b)] and leads to the formation of von Kármán vortex street [Bénard (1908); von Kármán (1911); Jackson (1987)]. It was first observed by Lord Rayleigh [Rayleigh (1945)] that the appearance of vortex street is related to the wake instability. The stability of the flow can be studied numerically via two procedures: Direct time integration (DTI) of flow equations or the Linear stability analysis (*LSA*). *LSA* has been utilized by various researchers in the past to investigate the stability of bluff body flows. Usually one of the two approaches is undertaken: the local analysis via parallel flow approximation or the global non-parallel flow approach. In the local approach a parallel flow approximation is considered at various stations in the flow field. Depending on whether the flow is assumed to be viscous or inviscid the Orr-Sommerfeld or the Rayleigh equation [Drazin and Reid (1981)] is utilized. Further, the absolute/convective nature of the instability is determined at various locations in the flow field. It is widely accepted that a global instability appears only when a substantial region of the flow field becomes locally absolutely unstable [Huerre and Monkewitz (1990)]. In the non-parallel flow approach, the nature of disturbance is global. The linearized Navier-Stokes equations are used to determine the onset of instability. Winters *et al*. [Winters et al (1986)] were the first to utilize this approach to analyze the stability of flow past a cylinder. They used a finite element formulation to determine the critical Reynolds number and vortex shedding frequency. Later, *LSA* approach was used by many other researchers [Ding and Kawahara (1999); Jackson (1987); Morzynski and Thiele (1991); Morzynsk et al (1999)].

Several researchers in the past have reported the critical Reynolds number and the Strouhal number at the onset of unsteadiness in flow past a cylinder. A large variation in the reported data exists. For example, Zebib [Zebib (1987)], with a circular domain of radius $10D$, observed $Re_c = 39-43$ and $St_c = 0.11-0.13$. Morzynski *et al*. [Morzynsk et al (1999)], from computations on a domain of size $20D \times 10D$, reported $Re_c = 47.0$ and $St_c = 0.132$. Jackson [Jackson (1987)], using a domain of size $20D \times 10D$, found $Re_c = 45.403$. Kumar and Mittal [Kumar and Mittal (2006b)] carried out a systematic investigation of the effect of the location of lateral boundaries on the critical parameters. It was found that while the $Re_c$ shows a non-monotonic variation with the lateral width of the domain, the $St_c$ shows a monotonic trend. One of the important observations from their work, in the present context, is that the location of the lateral boundaries have a relatively significant

effect on the growth rate and frequency of the eigenmodes.

It is generally believed that the Kármán mode is the only unstable mode for the flow past a cylinder for $Re_c < Re < 180$. It is, however, interesting to investigate if the Kármán mode is the least stable mode for $Re < Re_c$ as well. Zebib [Zebib (1987)] addressed this question via a spectral method. He used trigonometric sine functions and Chebyshev polynomials as basis functions in the azimuthal and radial directions, respectively. From his linear stability analysis he discovered three modes in addition to the Kármán mode. Further, it was found that the $St = 0.06$ mode dominates the flow for $Re < 25$, approximately. For $Re > 25$, the mode with $St = 0.10$ is the one that is least stable. The Kármán mode with $St = 0.12$ is the least stable mode beyond $Re \sim 40$. The flow becomes unstable for $Re > 45$. It was also ascertained that a purely real mode, with growth rate of $-0.01$, exists for $Re < 60$.

The results from Zebib[Zebib (1987)] clearly show that modes other than the Kármán mode dominate the flow for $Re$ sufficiently smaller than the critical. However, the domain size considered in his study is rather small. The streamwise length of the domain might place a lower bound on the time frequency of the mode that can be realized in a computation. A larger domain size may facilitate the appearance of modes with lower frequency. In particular, we anticipate the presence of purely real modes that have growth rate comparable to the Kármán mode. In the present study we carry out computations with domains of much larger size ($100 \leq H/D \leq 3000$) in order to investigate the dynamics of mode competition. Here, $H$ is the length of the domain and $D$ is the diameter of the cylinder. Our preliminary computations show that the crossover occurs near the onset of vortex shedding. We, therefore, carry out detailed study of the flow for $Re = 45$ and 48. Most of the computations reported in the literature have employed a rectangular domain. In this study we consider a square domain to restrict the parameters related to domain size to one. The computational results from the various domain sizes is utilized to extrapolate the results for an infinite domain. These results are used to determine the $Re$ at which the crossover between various modes takes place.

The article is organized in the following manner. In the next section, the governing equations are presented. Section 3 presents the finite element formulation of the governing equation. The problem set-up and boundary conditions are described in section 4. Results and their discussion are presented in section 5. The paper closes with a summary in section 6.

## 2    The Governing Equations

### 2.1    *The Incompressible Flow Equations*

Let $\Omega \subset R^2$ be the spatial domain. The boundary of $\Omega$ is denoted by $\Gamma$ and is assumed to be piecewise smooth. The incompressible flow is governed by the equations for balance of forces and conservation of mass. These are given as:

$$\rho(\frac{\partial \mathbf{u}}{\partial t} + \mathbf{u} \cdot \boldsymbol{\nabla}\mathbf{u}) - \boldsymbol{\nabla} \cdot \boldsymbol{\sigma} = \mathbf{0} \qquad \text{on } \Omega \times (0, T), \tag{1}$$

$$\boldsymbol{\nabla} \cdot \mathbf{u} = 0 \qquad \text{on } \Omega \times (0, T). \tag{2}$$

Here $\rho$, $\mathbf{u}$ and $\boldsymbol{\sigma}$ are the density, velocity and the stress tensor, respectively. For a Newtonian fluid the stress tensor is given as the sum of its isotropic and deviatoric parts:

$$\boldsymbol{\sigma} = -p\mathbf{I} + 2\mu\boldsymbol{\varepsilon}(\mathbf{u}), \quad \boldsymbol{\varepsilon}(\mathbf{u}) = \frac{1}{2}((\boldsymbol{\nabla}\mathbf{u}) + (\boldsymbol{\nabla}\mathbf{u})^T). \tag{3}$$

The variables $p$, $\mu$ and $\boldsymbol{\varepsilon}$ represent the pressure, coefficient of dynamic viscosity and strain rate, respectively. Both, the Dirichlet and Neumann-type boundary conditions are accounted for and are represented as

$$\mathbf{u} = \mathbf{g} \text{ on } \Gamma_g, \quad \mathsf{n} \cdot \boldsymbol{\sigma} = \mathbf{h} \text{ on } \Gamma_h, \tag{4}$$

respectively, where $\Gamma_g$ and $\Gamma_h$ are complementary subsets of the boundary $\Gamma$, $\mathsf{n}$ is its unit normal vector and $\mathbf{h}$ is the surface traction vector. The details of the boundary and initial conditions used to solve equations (1) and (2) are described in section 4.

### 2.2    *The Linearized Disturbance Equations (LDE)*

The flow variables are expressed as a combination of the steady flow and the disturbance: $\mathbf{u} = \mathbf{U} + \mathbf{u}'$ and $p = P + p'$. Here, $(\mathbf{U}, P)$ represent the steady-state solution obtained by solving Eqs. (1) and (2) without the time dependent terms. $\mathbf{u}'$ and $p'$ are the perturbation fields of the velocity and pressure, respectively. Substituting for this decomposition in Eqs. $(1) - (2)$ and subtracting from them, the equations for steady flow, one obtains the equations for the disturbance field. It is further assumed that the disturbances are very small. Therefore, the non-linear term in the disturbance equations is dropped. This leads to the Linearized Disturbance Equations (LDE) of the form:

$$\rho(\frac{\partial \mathbf{u}'}{\partial t} + \mathbf{u}' \cdot \boldsymbol{\nabla}\mathbf{U} + \mathbf{U} \cdot \boldsymbol{\nabla}\mathbf{u}') - \boldsymbol{\nabla} \cdot \boldsymbol{\sigma}' = 0, \tag{5}$$

$$\boldsymbol{\nabla} \cdot \mathbf{u}' = 0. \tag{6}$$

Here, $\boldsymbol{\sigma}'$ is the stress tensor due to the perturbed solution $(\mathbf{u}', p')$ as given by Eq.(3).

### 2.3 Global Linear Stability Analysis (LSA) of the steady flow

For conducting linear stability analysis (LSA) it is assumed that the perturbations are of the following form:

$$\mathbf{u}'(\mathbf{x},t) = \hat{\mathbf{u}}(\mathbf{x})e^{\lambda t}, \qquad p'(\mathbf{x},t) = \hat{p}(\mathbf{x})e^{\lambda t}. \tag{7}$$

Substituting Eq. (7) in Eqs. (5) − (6), we get

$$\rho\left(\lambda\hat{\mathbf{u}} + \hat{\mathbf{u}}\cdot\boldsymbol{\nabla}\mathbf{U} + \mathbf{U}\cdot\boldsymbol{\nabla}\hat{\mathbf{u}}\right) - \boldsymbol{\nabla}\cdot\hat{\boldsymbol{\sigma}} = 0 \qquad \text{on } \Omega \tag{8}$$

$$\boldsymbol{\nabla}\cdot\hat{\mathbf{u}} = 0 \qquad \text{on } \Omega. \tag{9}$$

Here, $\lambda$ is the eigenvalue of the fluid system and governs its stability. In general $\lambda$ is a complex number. The solution $(\mathbf{U},P)$ is associated with an unstable mode if the corresponding eigenvalue, $\lambda$, has a positive real part. The imaginary part of $\lambda$ is related to the temporal frequency of the disturbance. The boundary conditions for $(\hat{\mathbf{u}}, \hat{p})$ are the homogeneous versions of the ones for $(\mathbf{U},P)$.

## 3 The Finite Element Formulation

### 3.1 The Incompressible Flow Equations

Consider a finite element discretization of the domain, $\Omega$, into subdomains $\Omega^e$, $e = 1, 2, ..., n_{el}$, where $n_{el}$ is the number of elements. Based on this discretization let $\mathscr{S}_{\mathbf{u}}^h$ and $\mathscr{S}_p^h$ be the finite element trial function spaces for velocity and pressure, respectively and $\mathscr{V}_{\mathbf{u}}^h$ and $\mathscr{V}_p^h$ be the weighting function spaces. The stabilized finite element formulation of Eqs. (1) − (2) is written as follows: find $\mathbf{u}^h \in \mathscr{S}_{\mathbf{u}}^h$ and $p^h \in \mathscr{S}_p^h$ such that $\forall\ \mathbf{w}^h \in \mathscr{V}_{\mathbf{u}}^h, q^h \in \mathscr{V}_p^h$

$$\int_\Omega \mathbf{w}^h \cdot \rho \left( \frac{\partial \mathbf{u}^h}{\partial t} + \mathbf{u}^h \cdot \boldsymbol{\nabla}\mathbf{u}^h \right) d\Omega + \int_\Omega \boldsymbol{\varepsilon}(\mathbf{w}^h) : \boldsymbol{\sigma}(p^h, \mathbf{u}^h) d\Omega$$

$$+ \int_\Omega q^h \boldsymbol{\nabla}\cdot\mathbf{u}^h d\Omega + \sum_{e=1}^{n_{el}} \int_{\Omega^e} \frac{1}{\rho} \left( \tau_{\text{SUPG}}\rho\mathbf{u}^h \cdot \boldsymbol{\nabla}\mathbf{w}^h + \tau_{\text{PSPG}}\boldsymbol{\nabla}q^h \right)\cdot$$

$$\left[ \rho \left( \frac{\partial \mathbf{u}^h}{\partial t} + \mathbf{u}^h \cdot \boldsymbol{\nabla}\mathbf{u}^h \right) - \boldsymbol{\nabla}\cdot\boldsymbol{\sigma}(p^h, \mathbf{u}^h) \right] d\Omega^e$$

$$+ \sum_{e=1}^{n_{el}} \int_{\Omega^e} \tau_{\text{LSIC}}\boldsymbol{\nabla}\cdot\mathbf{w}^h \rho\boldsymbol{\nabla}\cdot\mathbf{u}^h d\Omega^e = \int_{\Gamma_h} \mathbf{w}^h \cdot \mathbf{h}^h d\Gamma. \tag{10}$$

In the variational formulation given by Eq. (10), the first three terms and the right-

hand side constitute the Galerkin formulation of the problem. It is well known that the Galerkin formulation is unstable with respect to the advection operator as the cell Reynolds number (based on the local flow velocity and mesh size) becomes larger. Also, not all combinations of the velocity and pressure interpolations are admissible in the Galerkin formulation. Elements that do not satisfy the Babuska-Brezzi condition lead to oscillatory solutions and, sometimes, no solution at all. To give stability to the basic formulation, a series of element-level integrals are added. The first series of element-level integrals are the SUPG and PSPG stabilization terms added to the variational formulations (Tezduyar *et al.* 1992 [Tezduyar et al (1992)]). The SUPG formulation for convection dominated flows was introduced by Hughes and Brooks [Hughes and Brooks (1979)] and Brooks and Hughes [Brooks and Hughes (1982)]. The Petrov-Galerkin term for Stokes flows, to admit the use of equal-order interpolations for velocity and pressure without producing oscillations in the pressure field, was proposed by Hughes *et al.* [Hughes et al (1986)]. Tezduyar *et al.* [Tezduyar et al (1992)] proposed a formulation using the SUPG and PSPG stabilizations for finite Reynolds number flows. The second series of element level integrals are stabilization terms based on the least squares of the divergence-free condition on the velocity field. The definition for $\tau_{\text{PSPG}}$ and $\tau_{\text{SUPG}}$ is given by the following relations based on its values for the advection and diffusion limits.

$$\tau_{\text{SUPG}} = \tau_{\text{PSPG}} = \left( \frac{1}{\tau_{\text{ADV}}^2} + \frac{1}{\tau_{\text{DIF}}^2} \right)^{-\frac{1}{2}}, \tag{11}$$

where,

$$\tau_{\text{ADV}} = \frac{h^e}{2\|\mathbf{u}^h\|}, \tau_{\text{DIF}} = \frac{(h^e)^2}{12\nu}. \tag{12}$$

Here, $h^e$ is the element length and various definitions have been used by researchers in the past. Mittal [Mittal (2000)] conducted a systematic numerical study to investigate the effect of high aspect ratio elements on the performance of the finite element formulation for three commonly used definitions of $h^e$. In this work we use the definition based on the minimum edge length of an element. The coefficient $\tau_{\text{LSIC}}$ is defined as

$$\tau_{\text{LSIC}} = \left( \frac{1}{\delta_{\text{ADV}}^2} + \frac{1}{\delta_{\text{DIF}}^2} \right)^{-\frac{1}{2}}, \tag{13}$$

where

$$\delta_{\text{ADV}} = \frac{h^e \|\mathbf{u}^h\|}{2}, \delta_{\text{DIF}} = \frac{(h^e)^2 (\|\mathbf{u}^h\|)^2}{12\nu}. \tag{14}$$

The linear equation system resulting from the finite element discretization of the flow equations are solved using the Generalized Minimal RESidual (GMRES) technique [Saad and Schultz (1986)] in conjunction with diagonal preconditioners. The implicit method used in the present work allows us to seek steady-state solutions by simply dropping the unsteady terms in the governing equations.

### 3.2 The Linear Stability Equations

Let $\hat{\mathscr{S}}_{\mathbf{u}}^h$ and $\hat{\mathscr{S}}_p^h$ be the finite element trial function spaces and $\hat{\mathscr{V}}_{\mathbf{u}}^h$ and $\hat{\mathscr{V}}_p^h$ the weighting function spaces for the perturbations in the velocity and pressure fields, respectively. The finite element formulation for the perturbation equations, (8) and (9), is given as: find $\hat{\mathbf{u}}^h \in \hat{\mathscr{S}}_{\mathbf{u}}^h$ and $\hat{p}^h \in \hat{\mathscr{S}}_p^h$ such that $\forall\ \hat{\mathbf{w}}^h \in \hat{\mathscr{V}}_{\mathbf{u}}^h$ and $\hat{q}^h \in \hat{\mathscr{V}}_p^h$

$$
\int_\Omega \hat{\mathbf{w}}^h \cdot \rho \left( \lambda \hat{\mathbf{u}}^h + \mathbf{U}^h \cdot \boldsymbol{\nabla} \hat{\mathbf{u}}^h + \hat{\mathbf{u}}^h \cdot \boldsymbol{\nabla} \mathbf{U}^h \right) d\Omega + \int_\Omega \boldsymbol{\varepsilon}(\hat{\mathbf{w}}^h) : \boldsymbol{\sigma}(\hat{p}^h, \hat{\mathbf{u}}^h) d\Omega
$$

$$
+ \int_\Omega \hat{q}^h \boldsymbol{\nabla} \cdot \hat{\mathbf{u}}^h d\Omega + \sum_{e=1}^{n_{el}} \int_{\Omega^e} \frac{1}{\rho} \left( \tau_{\mathrm{SUPG}} \rho \mathbf{U}^h \cdot \boldsymbol{\nabla} \hat{\mathbf{w}}^h + \tau_{\mathrm{PSPG}} \boldsymbol{\nabla} \hat{q}^h \right) \cdot
$$

$$
\left[ \rho \left( \lambda \hat{\mathbf{u}}^h + \mathbf{U}^h \cdot \boldsymbol{\nabla} \hat{\mathbf{u}}^h + \hat{\mathbf{u}}^h \cdot \boldsymbol{\nabla} \mathbf{U}^h \right) - \boldsymbol{\nabla} \cdot \boldsymbol{\sigma}(\hat{p}^h, \hat{\mathbf{u}}^h) \right] d\Omega^e
$$

$$
+ \sum_{e=1}^{n_{el}} \int_{\Omega^e} \tau_{\mathrm{LSIC}} \boldsymbol{\nabla} \cdot \hat{\mathbf{w}}^h \rho \boldsymbol{\nabla} \cdot \hat{\mathbf{u}}^h d\Omega^e = 0. \tag{15}
$$

The stabilization coefficients for the linear stability analysis are given by the same definition as defined in Eqs. $(11) - (14)$ except that they are based on the steady-state velocity field, $\mathbf{U}^h$. Eq. (15) leads to a generalized eigenvalue problem of the form $\mathbf{A}X - \lambda \mathbf{B}X = 0$, where $\mathbf{A}$ and $\mathbf{B}$ are non symmetric matrices. Various algorithms have been developed, in the past, to solve such eigenvalue problems with large sparse non symmetric matrices. For example, some of the methods are the inverse iteration [Wilkinson (1965)], subspace/simultaneous iteration [Stewart (1976)], Lanczos method [Meyer (1987)] and Arnoldi method [Arnoldi (1951)]. In the present case, the situation is complicated by the fact that the continuity equation, which is responsible for determining the pressure, causes the matrix $\mathbf{B}$ to become singular. Fortunately, in the context of linear stability analysis, we only need to track the leading/rightmost eigenvalue (the eigenvalue with the largest real part). In this study we use the shift-invert transformation in conjunction with the subspace iteration method [Stewart (1975)] and the Arnoldi method. The eigenfunctions are normalized such that the Euclidean norm of the vector formed of the values of velocity and pressure, of the real as well as imaginary components at all nodes, is unity.
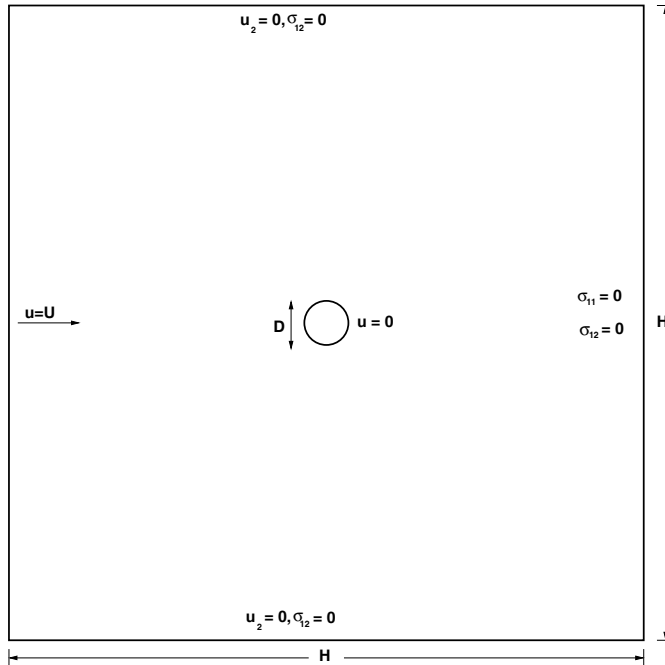
Figure 1: Flow past a cylinder: schematic and the problem set-up.

## 4   Problem set-up and boundary conditions

Figure 1 shows a schematic of the problem set-up. The circular cylinder resides in a computational domain whose outer boundary is a square. The center of the cylinder is placed at the origin. The radius of the cylinder is one unit; time is non-dimensionalized using the free-stream speed and the radius of the cylinder. The figure also shows the boundary conditions used for computing the flow. Free-stream value is assigned to the velocity at the upstream boundary. At the downstream boundary, a Neumann-type boundary condition for the velocity is specified that corresponds to zero stress vector. On the upper boundary a "slip-wall" boundary condition is employed, i.e., the component of velocity normal to and the component of stress vector along the boundary are prescribed a zero value. For the linear stability analysis, the boundary conditions on the perturbations are the homogeneous versions of the ones used for determining the steady state solution.

The finite element mesh is partitioned in two regions: an inner square region that surrounds the cylinder and an outer region. A typical mesh employed in the computation is shown in Figure 2. $H$ represents the edge-length of the outer boundary

while $S$ denotes the edge-length of the inner square box. The inner box has sufficient number of grid points to resolve the boundary layer. We generate finite element meshes for various values of $H$. In all cases the grid inside the square box, of dimension $S/D = 2$, is identical.
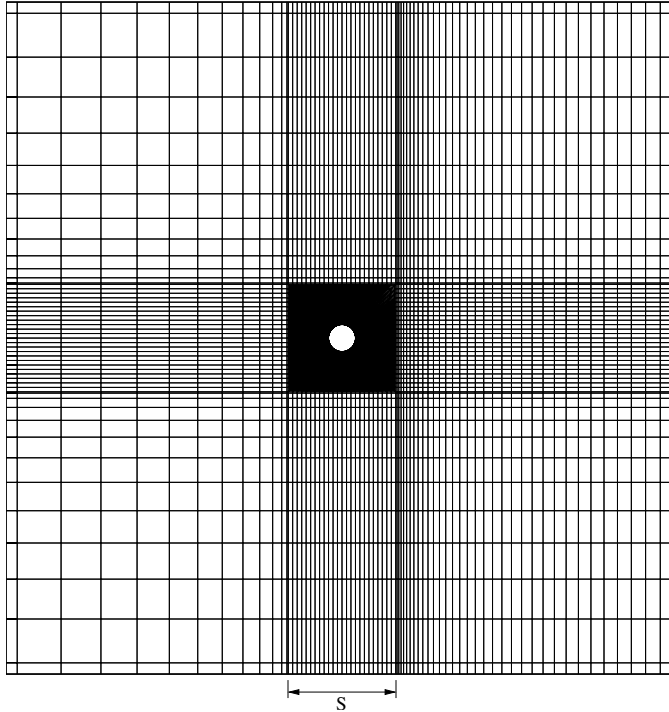


Figure 2: Flow past a cylinder: close-up view of the finite element mesh.

## 5   Results

### 5.1   The steady flow

The steady flow is computed by dropping the time dependent terms from Eqs. $(1) - (2)$. The nonlinear algebraic equation system arising from the finite element discretization is solved via the Newton-Raphson technique. A direct method is utilized to solve the linearized equation system. The top frame in Figure 3 shows the vorticity field of the steady flow for $Re = 45$ and $H/D = 200$. The flow is symmetric about the wake centre line. In all the figures in this paper black color

represents negative while the white represents positive values. Our steady flow results are in excellent agreement with the results reported by other researchers in the past. For example, the length of the recirculation bubble for $Re = 100$ from the present computations is $6.6378D$ and the drag coefficient is $0.5382$. These values from Fornberg [Fornberg (1991)] are $6.6D$ and $0.536$, respectively. Gajjar and Azzam [Gajjar and Azzam (2004)] reported these values to be $6.64D$ and $0.5395$.
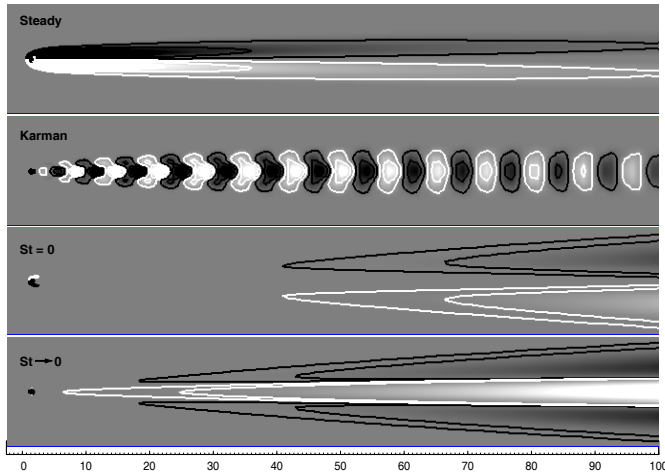


Figure 3: $Re = 45$, $H/D = 200$ flow past a circular cylinder: vorticity fields for (*i*) steady flow, (*ii*) Kármán mode, (*iii*) $St = 0$ mode and (*iv*) $St \rightarrow 0$ mode. Black color represents negative while the white represents positive values.

## 5.2   *Linear stability analysis* (*LSA*)

### 5.2.1   *The most unstable modes*

The global linear stability analysis of the steady flow is carried out at different $Re$ for various domain sizes. Beyond the critical Reynolds number, $Re_c$, the steady state is unstable. The $Re_c$ for flow past a cylinder is $\sim 47$ [Kumar and Mittal (2006b)]. For $Re < Re_c$ our analysis shows that, in addition to the Kármán mode, two additional modes have comparable growth rate. While one is a purely real mode, the other is a very low frequency mode. The vorticity field of the leading eigenmodes at $Re = 45$ for $H/D = 200$ are shown in Figure 3. The second row in Figure 3 shows the Kármán mode. The mode shown in the third row of Figure 3 is a purely real mode ($St = 0$) and its vorticity field is skew-symmetric with respect to wake central line. The bottom-most frame in Figure 3 shows the vorticity field for the real part of the complex eigenmode. The eigenfrequency of this mode is

Table 1: Mesh convergence: Information on various mesh used for $Re = 45$ and $H/D = 150$.

| Mesh | $N_{nod}$ | $N_{el}$ | $N_R$ | $N_T$ | $N_{X_R}$ | $N_{Y_U}$ | $N_{Y_L}$ | $\lambda_{r_{St=0}}$ | $\lambda_{r_{St \to 0}}$ |
|------|-----------|----------|-------|-------|-----------|-----------|-----------|----------------------|--------------------------|
| $M1$ | 19743 | 19420 | 26 | 24 | 113 | 38 | 38 | $-0.02415$ | $-0.02892$ |
| $M2$ | 29843 | 29420 | 26 | 24 | 213 | 38 | 38 | $-0.02415$ | $-0.02892$ |
| $M3$ | 45903 | 45388 | 61 | 72 | 113 | 38 | 38 | $-0.02422$ | $-0.02893$ |
| $M4$ | 110888 | 110080 | 52 | 48 | 426 | 76 | 76 | $-0.02421$ | $-0.02894$ |

$N_{nod}$ and $N_{el}$ are the total number of nodes and elements in the domain, respectively. $N_R$, $N_T$ are the number of points in radial and tangential direction inside the box surrounding the cylinder, respectively. $N_{X_R}$ is the number of points in the streamwise direction downstream of the cylinder. $N_{Y_U}$ and $N_{Y_L}$ are the number of points outside the inner box in the lateral direction above and below the cylinder, respectively.

very small. We denote this very low frequency mode by the $St \to 0$ mode. The vorticity fields of $St \to 0$ and Kármán modes are symmetric with respect to free stream velocity direction.

### 5.2.2  Mesh convergence

The adequacy of the mesh being used for the present study is tested by carrying out computations over a series of finite element mesh with varied resolution. The computations are carried out for $Re = 45$ and $H/D = 150$. Details of the various meshes are given in Table 1. Mesh $M1$, the base mesh, consists of 19743 nodes and 19420 quadrilateral elements. Mesh $M2$ has higher resolution in the streamwise direction in the wake. Mesh $M3$ has more resolution inside the square box as compared to meshes $M1$ and $M2$. Mesh $M4$ has an overall increased resolution in all directions. Table 1 shows the growth rate obtained with the four meshes for the two modes with rightmost eigenvalues, *i.e.*, the modes with eigenvalues that have the largest real part. It is observed from this table that the results from all the four meshes are in excellent agreement. The difference in the various results is less than 0.25%. Therefore, for the remaining computations reported in the paper, we utilize meshes that have the same spatial resolution as mesh $M1$.
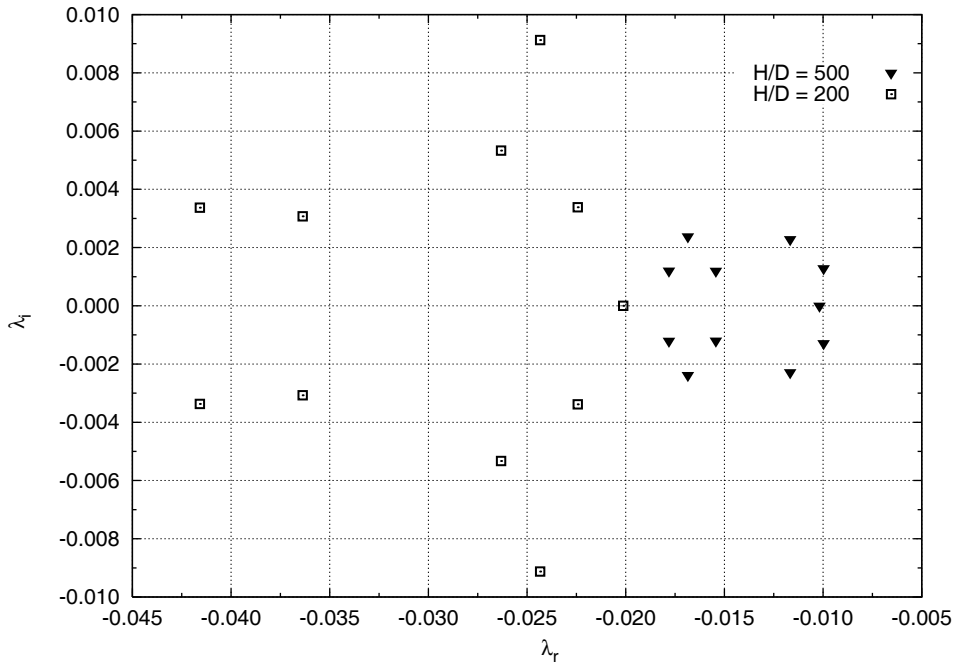
Figure 4: *Re* = 45 flow past a circular cylinder: the distribution of eigenvalues for $H/D = 200$ and 500. The KárMán mode is the right most mode for both values of $H/D$. However, it does not show up in the figure since its imaginary part is much larger than the extent of *y*-axis.
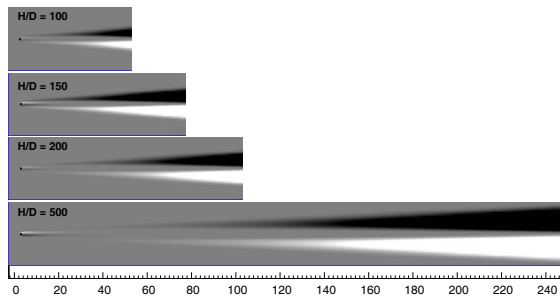


Figure 5: *Re* = 45 flow past a circular cylinder: vorticity fields for $St = 0$ modes. Black color represents negative while the white represents positive values.

### 5.2.3  *Effect of $H/D$*

Figure 4 illustrates the distribution of eigenvalues of various modes for two different domain sizes: $H/D = 200$ and 500. From this figure, it is observed that the
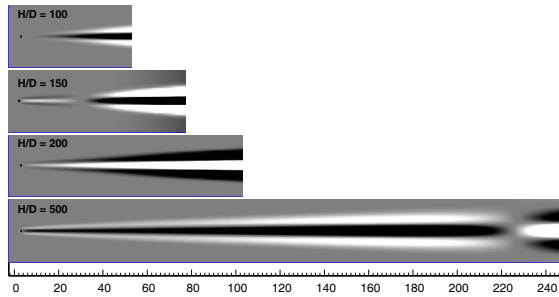
Figure 6: $Re = 45$ flow past a circular cylinder: vorticity fields for $St \rightarrow 0$ modes. Black color represents negative while the white represents positive values.

eigenmodes are less stable for larger domain size. Also, the imaginary part of the eigenvalue, that is related to $St$, decreases with increase in $H/D$. Shown in Figures 5 and 6 are the vorticity fields for these modes for four different values of $H/D$. The observations from Figures 4, 5 and 6 consistently show that the modes seem to adjust to the spatial extent of the domain. The $St = 0$ is shown in Figure 5 while the $St \rightarrow 0$ mode is presented in Figure 6. Both the modes are found to be very sensitive to the extent of spatial domain. Contrary to this behaviour, the Kármán mode is less sensitive. Recently Kumar and Mittal [Kumar and Mittal (2006b,a)] investigated the effect of blockage on the critical parameters for the flow past a circular cylinder. They showed that the $Re_c$ and $St_c$ remain almost unaffected for domain sizes larger than $100D$. It follows that the variation of growth rate and frequency of the Kármán mode are negligible, at least near the critical $Re$, for the domain sizes considered in this study.

To further investigate the effect of $H/D$ several finite element meshes, with various size of computational domain but the same resolution, are generated. For example, the mesh with $H/D = 100$ has $11,746$ nodes and $11,496$ quadrilateral elements while the one with $H/D = 200$ consist of $30,092$ nodes and $29,696$ quadrilateral elements. Computations are carried out on these modes for the $Re = 45$ and $48$ flow. The results from these computations are presented in Figures 7 and 8. These figures show the variation of $\lambda_r$ and $St$ with $H/D$ for the two rightmost eigenvalues. The Strouhal number for the $St \rightarrow 0$ mode decreases monotonically with $H/D$. A similar trend was observed by Behr *et al*. [Behr et al (1995)] and Kumar and Mittal [Kumar and Mittal (2006b)] for the Kármán mode. $\lambda_r$ is found to increase with $H/D$. Both, $\lambda_r$ and $St$ appear to achieve an asymptotic value as $H/D \rightarrow \infty$.
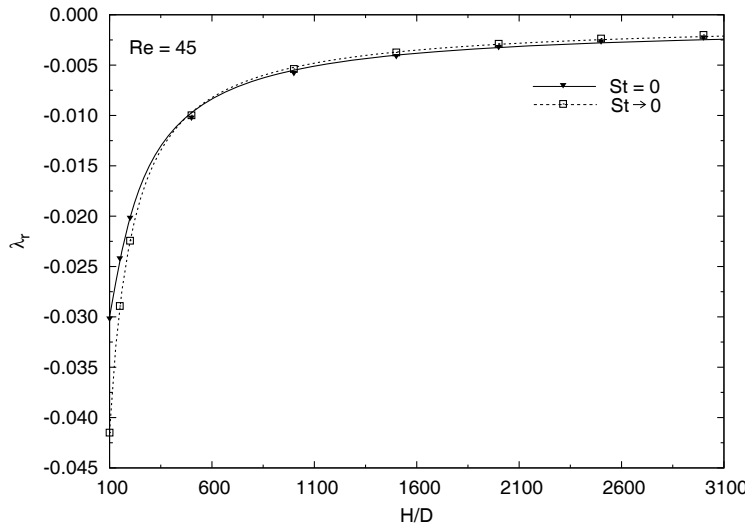
(a)
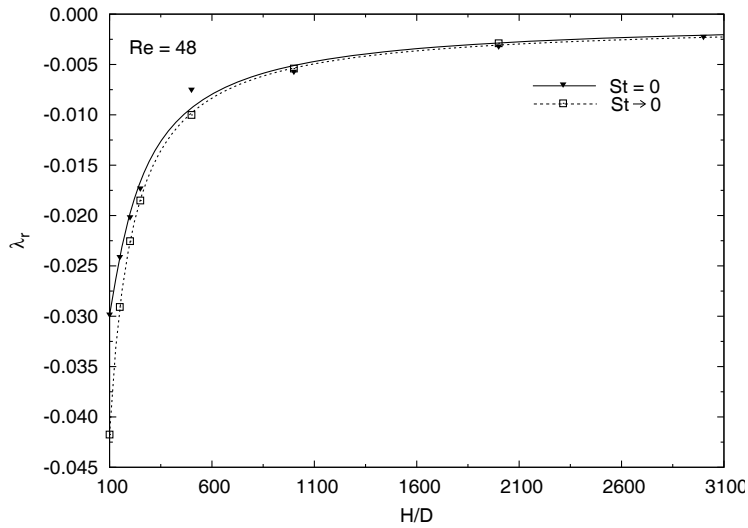


(b)

Figure 7: Linear stability analysis for flow past a circular cylinder: variation of the growth rate for the various modes with domain size for (a) *Re* = 45 and (b) *Re* = 48. The broken and solid lines show the best fit curve for *St* → 0 and *St* = 0, respectively.
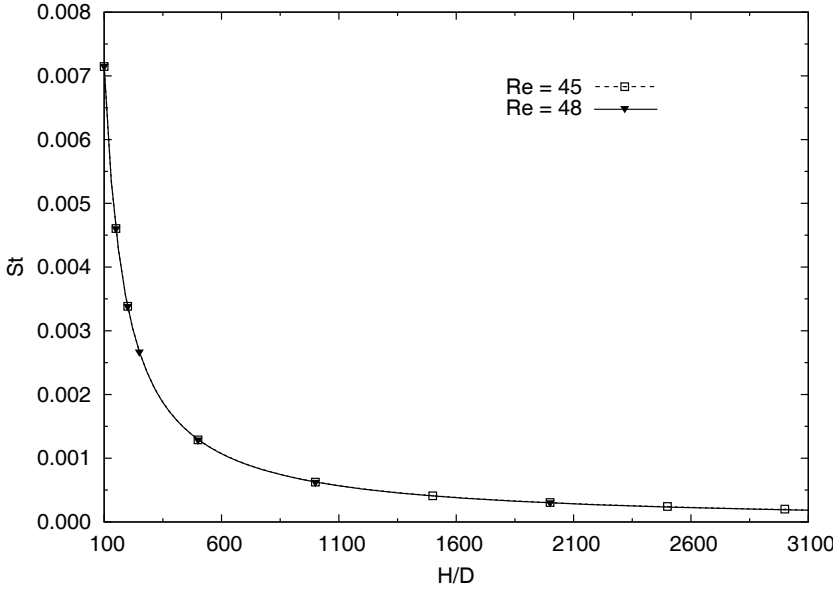
Figure 8: Linear stability analysis for flow past a circular cylinder: variation of the Strouhal number for the $St \to 0$ mode at $Re = 45$ and 48. The lines show the best fit curve.

### 5.3 Direct time integration (DTI) of linearized disturbance equation (LDE)

To confirm the correctness of the eigenvalues predicted from the global *LSA*, *DTI* of the *LDE* is carried out. The kinetic energy of the disturbance field, $\mathbf{u}'$, in the flow domain $\Omega$ is defined as $E(t) = \frac{\rho}{2} \int_\Omega \mathbf{u}' \cdot \mathbf{u}' d\Omega$. The eigenmode obtained from the global *LSA* of the steady flow is used as the disturbance field at $t = 0$. In this situation the kinetic energy can be expressed as $E(t) = \frac{\rho}{2} e^{2\lambda_r t} \int_\Omega \hat{\mathbf{u}} \cdot \bar{\hat{\mathbf{u}}} d\Omega$. Here, overbar indicates the complex conjugate, while $\lambda_r$ is the growth rate of the mode. This leads to the expression to estimate growth rate: $\lambda_r = \frac{1}{2t} ln \frac{E(t)}{E(0)}$.

The time evolution of the normalized kinetic energy, $E(t)/E(0)$, of the disturbance field is shown in Figure 9 on a log scale for the $Re = 45$ flow and $H/D = 1000$. Results are presented for time evolution of the energy for two simulations. The first one is for the purely real mode ($St = 0$). The second one is for the $St \to 0$ mode. In both the cases the slope of the energy curve is marked on the plot. Also marked is the slope expected from the *LSA* (slope $= 2\lambda_r$). Very good match is seen between the results from *LSA* and *DTI*. This increases our confidence in the results from the computations.
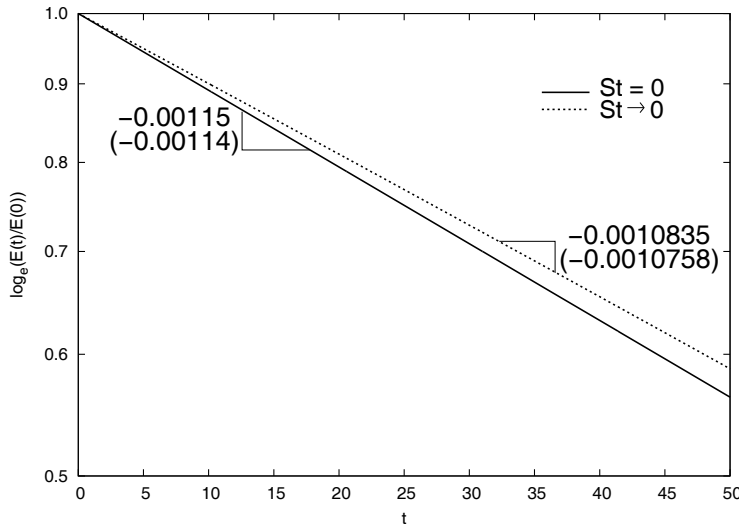
Figure 9: $Re = 45$, $H/D = 1000$ flow past a cylinder: time evolution of the normalized energy obtained by direct time integration of the linearized disturbance equations. The computations begin with the real part of the corresponding eigenmode obtained from global linear stability analysis (LSA). The slope shows the rate of change of $E(t)/E(0)$. Also shown in the parentheses is $2\lambda_r$ for the corresponding eigenmode obtained from LSA.

### 5.4  Estimation of $\lambda_r$ and St for unbounded flow

The blockage is defined as $B = D/H$. Utilizing the data shown in Figures 7 and 8 we attempt to estimate $\lambda_r$ and $St$ for $H/D \rightarrow \infty$. To this end, a curve fit, which is best in the sense of least-squares, is computed for the data. The curve fit is assumed to be of the following form:

$$\lambda_r, St = a + bB + cB^2. \tag{16}$$

The coefficients for the best fit, for $Re = 45$ and 48, are placed in Table 2. The variance of residual, $\sigma_{res}$, and $R^2$ for each fitment are also listed in the table. The residual for each data point is the difference between the observed and fitted response value. $R^2$ is the square of correlation between the two sets of values. We note that the coefficient $a$, in Eq. (16), corresponds to the value of the parameter $(\lambda_r, St)$ for an unbounded flow. The coefficient $a$ corresponding to $St$ for $H/D \rightarrow \infty$, for $Re = 45$ and 48 assume a value very close to zero. This confirms that this mode tends towards a purely real mode as the blockage reduces. The coefficient $a$ for
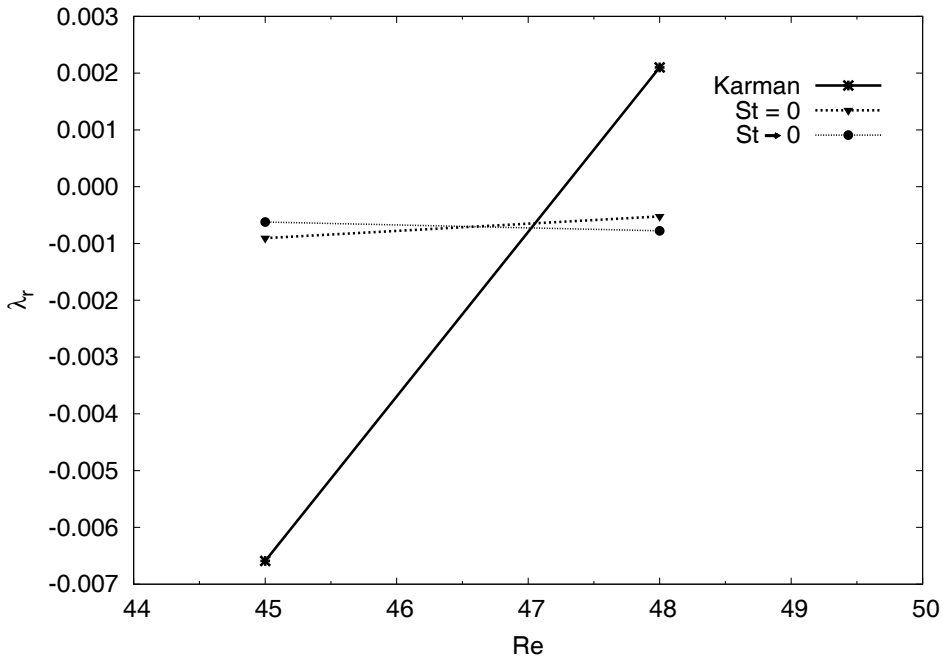
Figure 10: Flow past a circular cylinder: variation of the growth rate with *Re* for unbounded flow ($H/D \to \infty$) for various modes. The crossover of $St = 0$ mode with $St \to 0$ mode and $St \to 0$ mode with Kármán mode occurs at $Re = 44.02$ and $47.04$, respectively.

the growth rate, for all the modes, is also shown in Figure 10. This figure may be utilized to locate the *Re* at which the crossover of modes, with respect to being least stable, takes place. To estimate the *Re* for crossover, the variation of $\lambda_r$, for various modes, is assumed to be linear between $Re = 45$ and $48$. The $St \to 0$ mode is found to be the least stable mode for $46.59 \leq Re \leq 47.05$. For $Re \geq 47.05$ the Kármán mode is the one with rightmost eigenvalue. Interestingly, the growth rate of the Kármán mode increases very rapidly with *Re*. Consequently, it becomes unstable at a slightly higher *Re*. The present work does not address the relative stability of the modes for $Re < 45$. More crossovers are possible at lower *Re*. Zebib [Zebib (1987)] reported a crossover of modes close to the critical *Re* for onset of vortex shedding. For $25 < Re < 45$, the $St = 0.10$ mode was found to be least stable. The Kármán mode was found to be most unstable for $Re > 40$. The computations by Zebib [Zebib (1987)] were restricted to a relatively short domain. Therefore, it is quite likely the $St = 0$ and very low frequency modes were missed out in that study.

| | Mode | Re | a | b | c | $\sigma_{res}$ | $R^2$ |
|---|---|---|---|---|---|---|---|
| $\lambda_r$ | $St = 0$ | 45 | $-9.048 \times 10^{-4}$ | $-4.789$ | $187.92$ | $8.3159 \times 10^{-8}$ | $0.9994$ |
| | | 48 | $-5.235 \times 10^{-4}$ | $-4.764$ | $182.71$ | $8.8556 \times 10^{-7}$ | $0.9942$ |
| | $St \to 0$ | 45 | $-6.206 \times 10^{-4}$ | $-4.659$ | $57.968$ | $3.0409 \times 10^{-8}$ | $0.9999$ |
| | | 48 | $-7.755 \times 10^{-4}$ | $-4.629$ | $53.743$ | $2.7577 \times 10^{-8}$ | $0.9999$ |
| | Kármán | 45 | $-6.591 \times 10^{-3}$ | $0.053$ | $-0.3560$ | $3.4214 \times 10^{-12}$ | $0.9999$ |
| | | 48 | $2.101 \times 10^{-3}$ | $0.028$ | $4.0851$ | $3.9141 \times 10^{-10}$ | $0.9946$ |
| $St$ | $St \to 0$ | 45 | $-2.038 \times 10^{-5}$ | $0.644$ | $7.2525$ | $4.1627 \times 10^{-11}$ | $1$ |
| | | 48 | $-2.487 \times 10^{-5}$ | $0.645$ | $7.2769$ | $2.6232 \times 10^{-11}$ | $1$ |
| | $St_{Karman}$ | 45 | $1.154 \times 10^{-1}$ | $0.082$ | $-2.1567$ | $3.1041 \times 10^{-11}$ | $0.9994$ |
| | | 48 | $1.162 \times 10^{-1}$ | $-0.029$ | $13.084$ | $8.4909 \times 10^{-11}$ | $0.9992$ |

Table 2: Details of the coefficients for the best fit curve for different modes and at different Reynolds numbers.

## 6  Summary

Global linear stability analysis of the steady flow past a circular cylinder has been carried out for *Re* close to the onset of vortex shedding. In addition to the Kármán mode, which is responsible for vortex shedding, two other modes are tracked. One of them is a real mode while the other is associated with a very small imaginary part. The two modes are referred to as the $St = 0$ and $St \to 0$ modes, respectively. The vorticity field for the $St = 0$ mode is skew-symmetric, while it is symmetric for the $St \to 0$ mode, with respect to wake centre line. Unlike the Kármán mode, the growth rate of both these modes as well as the imaginary part of the complex mode is found to be very sensitive to the spatial extent of the computational domain. Therefore, computations are carried out for $Re = 45$ and 48 for domains of increasing spatial extent and the results are extrapolated to estimate the parameters for an unbounded domain. All the modes are stable for the $Re = 45$ flow while the Kármán mode is the only unstable mode for $Re = 48$. Of the three modes, the Kármán mode is most stable for the $Re = 45$ flow while the $St \to 0$ mode is least stable. For the $Re = 48$ flow, the $St \to 0$ mode is most stable followed by the $St = 0$ mode. The growth rate of all the modes is assumed to vary linearly between $Re = 45$ and 48. This variation is utilized to determine the relative stability of the three modes. The Kármán mode is the dominant mode for $Re \geq 47.05$ while the $St \to 0$ mode is

the least stable mode for $Re \leq 46.59$. The $St = 0$ mode has the largest growth rate for $46.59 < Re < 47.05$. The results from the LSA are confirmed via direct time integration ($DTI$) of the linearized equations. The estimate of growth rate from $DTI$ is in good agreement with the results from LSA. Other cross-overs of modes are possible at lower $Re$. However, that has not been explored in the study.

## References

**Arnoldi, W. E.** (1951): The principle of minimized iterations in the solution of the matrix eigenvalue problem. *Quart. Appl. Math.*, 9(MR 13:163e):17–29.

**Behr, M.; Hastreiter, D.; Mittal, S.; Tezduyar, T. E.** (1995): Incompressible flow past a circular cylinder: dependence of the computed flow field on the location of lateral boundaries. *Computer Methods in Applied Mechanics and Engineering*, 123:309–316.

**Bénard, H.** (1908): Formation de centres de giration á l'arriére d'un obstacle en mouvement. *C. R. Acad. Sci. Paris*, 147:839–842.

**Brooks, A.N.; Hughes, T. J. R.** (1982): Streamline upwind/Petrov-Galerkin formulations for convection dominated flows with particular emphasis on the incompressible Navier-Stokes equations. *Computer Methods in Applied Mechanics and Engineering*, 32:199–259.

**Ding, Y.; Kawahara, M.** (1999): Three dimensional linear stability analysis of incompressible viscous flows using the finite element method. *International Journal for Numerical Methods in Fluids*, 31:451–479.

**Drazin, P. G.; Reid, W. H.** (1981): *Hydrodynamic Stability*. Cambridge University Press, Cambridge, first edition.

**Fornberg, B.** (1991): Steady incompressible flow past a row of circular cylinders. *Journal of Fluid Mechanics*, 225:655–671.

**Gajjar, J. S. B.; Azzam, N. A.** (2004): Numerical solution of the Navier-Stokes equations for the flow in a cylinder cascade. *Journal of Fluid Mechanics*, 520:51–82.

**Huerre, P.; Monkewitz, P. A.** (1990): Local and global instabilities in spatially developing flows. *Annu. Rev. Fluid Mech.*, 22:473–537.

**Hughes, T. J. R.; Brooks, A.H.** (1979):   A multi-dimensional upwind scheme with no crosswind diffusion. In T.J.R. Hughes, editor, *Finite Element Methods for Convection Dominated Flows*, pages 19–35. ASME, New York.

**Hughes, T. J. R.; Franca, L. P.; Balestra, M.** (1986):   A new finite element formulation for computational fluid dynamics: V. Circumventing the Babuška–Brezzi condition: A stable Petrov–Galerkin formulation of the Stokes problem accommodating equal-order interpolations. *Computer Methods in Applied Mechanics and Engineering*, 59:85–99.

**Jackson, C. P.** (1987):   A finite-element study of the onset of vortex shedding in flow past variously shaped bodies. *Journal of Fluid Mechanics*, 182:23–45.

**Kumar, B.; Mittal, S.** (2006a:   Effect of blockage on critical parameters for flow past a circular cylinder. *International Journal for Numerical Methods in Fluids*, 50:987–1001.

**Kumar, B.; Mittal, S.** (2006b):   Prediction of the critical reynolds number for flow past a circular cylinder. *Computer Methods in Applied Mechanics and Engineering*, 195:6046–6058.

**Meyer, A.** (1987):   Algorithms for large sparse eigenvalue problems. *Akademie-Verlag*.

**Mittal, S.** (2000):   On the performance of high aspect-ratio elements for incompressible flows. *Computer Methods in Applied Mechanics and Engineering*, 188:269–287.

**Morzynski, M.; Thiele, F.** (1991):   Numerical stability analysis of a flow about a cylinder. *Zeitschrift fuer angewandte Mathematik und Mechanik*, 71:T424–T428.

**Morzynski, M.; Afanasiev, K.; Thiele, F.** (1999):   Solution of the eigenvalue problems resulting from global non-parallel flow stability analysis. *Computer Methods in Applied Mechanics and Engineering*, 169:161–176.

**Rayleigh, L.** (1945):   *Theory of sound*, volume II. Dover Publication, New York.

**Saad, Y.; Schultz, M. H.** (1986):   GMRES: A generalized minimal residual algorithm for solving nonsymmetric linear systems. *SIAM Journal of Scientific and Statistical Computing*, 7:856–869.

**Stewart, G. W.** (1976):   Simultaneous iteration for computing invariant subspaces of non hermitian matrices. *Numerische Mathematik*, 25:123–136.

**Stewart, G. W.** (1975):   Methods of simultaneous iteration for calculating eigenvectors of matrices. *Topics in Numerical Analysis II(ed. J.H.H. Miller),Academic*, pages 169–185.

**Tezduyar, T. E.; Mittal, S.; Ray, S. E.; Shih, R.** (1992): Incompressible flow computations with stabilized bilinear and linear equal-order-interpolation velocity-pressure elements. *Computer Methods in Applied Mechanics and Engineering*, 95:221–242.

**von Kármán, T.** (1911): Über den mechanismus des widerstandes, den ein bewegter körper in einer flüssigkeit erfährt. *Göttingen Nachr. Math.-Phys. Kl.*, 12:509–519.

**Winters, K.H.; Cliffe, K. A.; Jackson, C. P.** (1986): *The Prediction of Instabilities Using Bifurcation Theory*. Wiley, New York.

**Wilkinson, J. H.** (1965): *The Algebraic Eigenvalue Problem*. Clarendon Press, Oxford.

**Zebib, A.** (1987): Stability of viscous flow past a circular cylinder. *Journal of Engineering Mathematics*, 21:155–165.